

Tail-Aware Post-Training Quantization for 3D Geometry Models

Sicheng Pan ^{*1} Chen Tang ^{*2} Shuzhao Xie ^{*1} Ke Yang ³ Weixiang Zhang ¹ Jiawei Li ⁴
 Bin Chen ³ Shu-Tao Xia ¹ Zhi Wang ¹

Abstract

The burgeoning complexity and scale of 3D geometry models pose significant challenges for deployment on resource-constrained platforms. While Post-Training Quantization (PTQ) enables efficient inference without retraining, conventional methods, primarily optimized for 2D Vision Transformers, fail to transfer effectively to 3D models due to intricate feature distributions and prohibitive calibration overhead. To address these challenges, we propose **TAPTQ**, a Tail-Aware Post-Training Quantization pipeline specifically engineered for 3D geometric learning. Our contribution is threefold: (1) To overcome the data-scale bottleneck in 3D datasets, we develop a progressive coarse-to-fine calibration construction strategy that constructs a highly compact subset to achieve both statistical purity and geometric representativeness. (2) We reformulate the quantization interval search as an optimization problem and introduce a ternary-search-based solver, reducing the computational complexity from $\mathcal{O}(N)$ to $\mathcal{O}(\log N)$ for accelerated deployment. (3) To mitigate quantization error accumulation, we propose TRE-Guided Module-wise Compensation, which utilizes a Tail Relative Error (TRE) metric to adaptively identify and rectify distortions in modules sensitive to long-tailed activation outliers. Extensive experiments on the VGGT and Pi3 benchmarks demonstrate that TAPTQ consistently outperforms state-of-the-art PTQ methods in accuracy while significantly reducing calibration time. The code will be released soon.

1. Introduction

The emergence of large-scale 3D foundation models (Wang et al., 2024; Leroy et al., 2024; Wang et al., 2025b; Lin et al., 2025) has revolutionized the field of computer vision

by enabling end-to-end geometric learning directly from massive datasets. This paradigm shift addresses the fundamental challenge of inferring 3D structures from 2D images, which is a cornerstone task that has traditionally relied on Structure-from-Motion (SfM) pipelines (Cui et al., 2017; Schonberger & Frahm, 2016). By employing unified, feed-forward architectures, these modern models jointly solve diverse tasks like multi-view reconstruction and camera estimation with unprecedented accuracy. These advances hold immense potential for real-world applications in augmented reality (AR), autonomous driving, and robotics. However, the superior performance of these models is inextricably tied to their burgeoning scale, which results in massive computational and memory footprints. This presents significant hurdles for practical deployment on resource-constrained or latency-sensitive edge platforms.

Post-training Quantization (PTQ) (Wei et al., 2022; Frantar et al., 2022; Yuan et al., 2022) has emerged as a pivotal technique for model compression, facilitating the conversion of high-precision weights and activations into low-bit integer arithmetic without exhaustive retraining. While PTQ has achieved remarkable success in Large Language Models (LLMs) and 2D Vision Transformers (ViTs), a systematic investigation into its efficacy for 3D geometry foundation models remains largely underexplored. Our experimental results show that directly transplanting established PTQ recipes from the 2D vision to 3D geometry transformers leads to severe performance degradation and prohibitive calibration overhead. Such failures suggest that the unique properties and multi-view dependencies of 3D geometric data require a specialized quantization paradigm that goes beyond existing general-purpose frameworks.

We attribute these observed failures to the inherent differences of both 3D geometric data and model, which manifest as three primary obstacles: **First, statistical heterogeneity in multi-view calibration.** Unlike 2D image tasks, a single calibration instance in 3D geometry models typically comprises multiple correlated yet non-identical views. The resulting activation distributions are highly sensitive to viewpoint configurations and noisy geometric structures,

^{*}Equal contribution ¹Tsinghua Shenzhen International Graduate School, Tsinghua University, Shenzhen, China

²MMLab, The Chinese University of Hong Kong, Hong Kong, China ³Harbin Institute of Technology Shenzhen, China ⁴Huawei Technology, Shenzhen, China. Correspondence to: Bin Chen <chenbin2021@hit.edu.cn>, Zhi Wang <wangzhi@sz.tsinghua.edu.cn>.

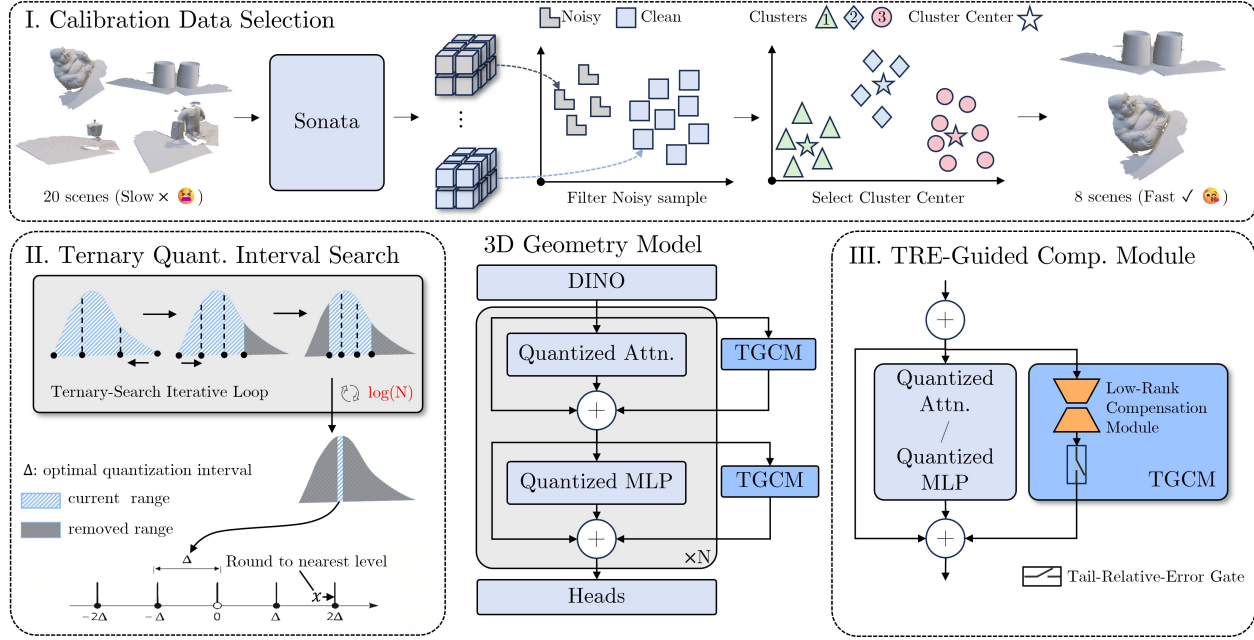


Figure 1. Overview of TAPTO. (I) Our proposed Representative Calibration Data via Two-Stage Cluster. (II) Our proposed Quantization Interval Optimization via Ternary Search. (III) Our proposed Tail-Relative-Error (TRE)-Guided Compensation Module.

leading to substantial inter-sample statistical variance. Consequently, a sparse calibration set may fail to encapsulate the underlying data manifold, causing range estimation to be biased by unstable outliers. While recent work (Feng et al., 2025) attempts to mitigate this through model-dependent filtering, such approaches often necessitate auxiliary forward passes and lack cross-architecture portability. **Second, the computational bottleneck of range optimization.** High-fidelity PTQ relies on optimizing clipping ranges or scaling factors via iterative evaluations. In 3D geometry settings, this cost is severely exacerbated by the multi-view inference paradigm and massive token sequences (e.g., dense point maps), rendering standard $\mathcal{O}(N)$ grid searches or reconstruction-based optimizations (e.g., BRECQ (Li et al., 2021)) computationally prohibitive. This necessitates a more efficient, ideally logarithmic-complexity search paradigm to accelerate calibration without sacrificing quantization fidelity. **Third, intensified error sensitivity in multi-task geometric inference.** Unlike previous architecture (e.g., 2D classification via ViTs), which exhibits higher tolerance to quantization noise, 3D geometry foundation naturally models demand significantly more stringent numerical precision. In complex tasks such as camera pose estimation and dense reconstruction, even minor quantization errors can amplify across transformer layers, leading to significant geometric drift and misalignment. This necessitates a principled and lightweight metric to selectively identify and rectify “bottleneck” modules to ensure geometric fidelity with minimal compensation overhead.

To address these challenges, we propose **TAPTO** (Tail-Aware Post-Training Quantization), a high-efficiency pipeline specifically tailored for 3D geometry models. TAPTO is built upon three core innovations: **(i) Progressive calibration set construction:** To ensure robustness under constrained data budgets, we develop a progressive coarse-to-fine calibration construction strategy to construct a compact yet statistically representative calibration set. This strategy suppresses the influence of unstable samples and noisy geometric structures, providing a solid foundation for consistent range estimation. **(ii) Ternary-search-based interval optimization:** We reformulate quantization interval selection as an optimization problem. By exploiting the near-unimodal property of the calibration objective, we introduce a ternary-search-based solver that reduces the search complexity from $\mathcal{O}(N)$ to $\mathcal{O}(\log N)$, significantly accelerating the deployment process without compromising quantization fidelity. **(iii) TRE-Guided Module-wise Compensation:** To mitigate error accumulation across transformer layers, we propose a selective compensation mechanism. We introduce the Tail Relative Error (TRE) metric to quantify distortions in high-magnitude activation regions. TRE acts as a gating criterion to adaptively identify and rectify only the most affected “bottleneck” modules, preserving geometric consistency with minimal computational overhead.

Our contributions are summarized as follows:

- We analyze why existing PTQ pipelines for LLMs and 2D vision transformers do not directly translate

to 3D geometry transformers, emphasizing calibration fragility, interval-search cost, and the need for selective error correction.

- We adopt a progressive coarse-to-fine calibration construction strategy that constructs a compact yet robust calibration set under limited calibration budgets.
- We introduce a ternary-search-based interval calibration method that reduces the interval-search complexity from $O(N)$ to $O(\log N)$.
- We propose TRE-Guided Module-wise Compensation, using Tail Relative Error to selectively activate compensation and mitigate cross-layer error accumulation with minimal overhead.

2. Related Work

2.1. Feed-forward 3D Geometry Models

Traditional 3D reconstruction typically follows a two-stage paradigm: Structure-from-Motion (SfM) for pose estimation followed by Multi-View Stereo (MVS) for dense geometry (Schonberger & Frahm, 2016; Yao et al., 2018). While neural radiance fields (NeRF) (Mildenhall et al., 2021; Barron et al., 2021) and 3D Gaussian Splatting (Kerbl et al., 2023; Xie et al., 2024; 2025) have revolutionized high-fidelity rendering, they fundamentally rely on *per-scene optimization*, which is computationally prohibitive for large-scale, real-time applications. To circumvent this, recent research has shifted toward *feed-forward geometry foundation models*. DUS3R (Wang et al., 2024) and MAS3R (Leroy et al., 2024) pioneered direct geometry inference from unconstrained image collections by predicting dense pointmaps. VGGT (Wang et al., 2025b) further unified multiple geometric tasks within a monolithic transformer architecture. Subsequent works have explored architectural efficiency through permutation-equivariant designs (Wang et al., 2025c), unified depth-ray prediction (Lin et al., 2025), and attention sparsification (Wang et al., 2025a; Shen et al., 2025). Despite these algorithmic advances, the massive parameter count and memory footprint of these transformers remain a bottleneck for edge deployment, necessitating effective model compression.

2.2. Post-Training Quantization (PTQ)

PTQ enables model compression using limited calibration data without the need for high-cost quantization-aware training (QAT) (Gholami et al., 2022). Early methods focused on MSE-driven range clipping (Banner et al., 2019) or weight equalization (Nagel et al., 2019). To achieve lower bit-widths, reconstruction-based approaches like AdaRound (Nagel et al., 2020), BRECQ (Li et al., 2021), and QDrop (Wei et al., 2022) optimize rounding or local block-wise

behavior to minimize output distortion. The shift toward Transformer architectures introduced new challenges, specifically regarding non-linearities (Softmax/GELU) and heavy-tailed activation distributions. In the vision domain, methods such as PTQ4ViT (Yuan et al., 2022) and RepQ-ViT (Li et al., 2023c) address these through specialized scaling and re-parameterization. Similarly, for Large Language Models (LLMs), frameworks like GPTQ (Frantar et al., 2022), SmoothQuant (Xiao et al., 2023), and AWQ (Lin et al., 2024) leverage one-shot weight updates or activation migration to preserve model capacity. However, recent analysis (He et al., 2025) suggests that the efficacy of these methods is highly sensitive to the choice of calibration data. Quantizing large-scale 3D geometry transformers is an emergent and under-explored area. While QuantVGGT (Feng et al., 2025) provided a preliminary study on the sensitivity of 3D activations, it does not fully address the calibration inefficiency and the complex error accumulation inherent in multi-view geometry tasks. Unlike general-purpose PTQ for 2D ViTs or LLMs, our work explicitly targets the unique failure modes of 3D models—specifically the tail-dominated activation ranges and view-dependent calibration variability. By introducing a ternary-search-based optimization and a tail-relative error metric, we bridge the gap between high-performance geometry foundation models and efficient hardware deployment.

3. Method

3.1. Preliminary

Post-training quantization (PTQ) compresses a pretrained model into low-bit arithmetic without retraining, by quantizing weights and activations using a small unlabeled calibration set. In this work, we adopt twin uniform quantization (Yuan et al., 2022), which maps a real-valued tensor x to its quantized version x_q via

$$x_q = \begin{cases} \text{clip}\left(\left\lfloor \frac{x}{\Delta_{R_1}} \right\rfloor, q_{\min}, q_{\max} \right) \cdot \Delta_{R_1}, & x \in \mathcal{R}_1, \\ \text{clip}\left(\left\lfloor \frac{x}{\Delta_{R_2}} \right\rfloor, q_{\min}, q_{\max} \right) \cdot \Delta_{R_2}, & x \in \mathcal{R}_2. \end{cases} \quad (1)$$

where $\Delta > 0$ denotes the quantization interval (i.e., scaling factor) and $[q_{\min}, q_{\max}]$ are quantization ranges that are determined by the given bit-width setting.

The central goal of PTQ is to determine Δ , because a small interval leads to saturation while a large interval increases rounding error (Tang et al., 2022). PTQ therefore determines Δ by comparing the outputs of the quantized model with those of the full-precision model on calibration data. Given the calibration inputs \mathbf{x} and the model $\mathcal{F}(\cdot)$, let $\mathbf{y}_{\text{FP}} = \mathcal{F}(\mathbf{x})$ be the full-precision output and $\mathbf{y}_{\Delta} = \mathcal{F}(\mathbf{x}; \Delta)$ the corresponding quantized output using the quantization intervals

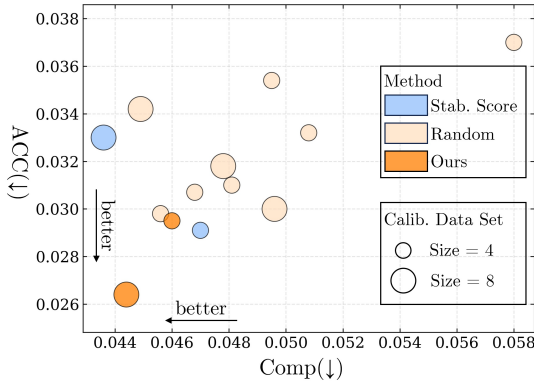


Figure 2. Acc. and Comp. performance under different calibration data set. Each bubble corresponds to one method configuration on 7Scenes (W4A8), where bubble size indicates the number of calibration samples (4 / 8 / 20 scans). *Stab. score* denotes a stability-based calibration sample selection strategy (see Appendix A.2).

Δ. Quantization interval optimization can be formulated as

$$\alpha^* = \arg \max_{\alpha \in \mathcal{A}} \text{Sim}(\mathbf{y}_{\text{FP}}, \mathbf{y}_\alpha), \quad (2)$$

where $\mathcal{A} = \{\alpha_i\}_{i=1}^N$ is a discrete set of candidate intervals and $\text{Sim}(\cdot)$ denotes a similarity metric, defined as

$$\text{Sim}(\mathbf{y}_{\text{FP}}, \mathbf{y}_\alpha) = -\|\mathbf{g} \odot (\mathbf{y}_{\text{FP}} - \mathbf{y}_\alpha)\|_2^2, \quad (3)$$

where \mathbf{g} is the gradient associated with the corresponding tensor, weighting quantization errors by local sensitivity.

Previous works (Yuan et al., 2022; Li et al., 2023a) evaluate all candidates in \mathcal{A} and thus incur $\mathcal{O}(N)$ forward passes, which becomes a major calibration bottleneck for large 3D geometry models. This motivates efficient interval search strategies for PTQ, which we address in the following section.

3.2. Progressive Calibration Set Construction

Post-training quantization relies heavily on the quality of the calibration set to estimate accurate quantization ranges. Conventional PTQ frameworks typically resort to random sampling (Wei et al., 2022; Frantar et al., 2022); however, we observe that for 3D geometry foundation models, such a stochastic approach leads to significant performance fluctuations. As demonstrated in Fig. 2, repeated random samplings result in a high variance of quantization accuracy, indicating that *unstable or noisy 3D samples can disproportionately distort the estimated quantization ranges*. To address this, we propose a progressive coarse-to-fine calibration construction strategy to achieve both *statistical purity* and *geometric representativeness*.

Stage 1: Coarse-grained Outlier Suppression. The initial stage aims to purify the calibration pool by filtering out

noisy instances. Given an unlabeled dataset $\mathcal{D} = \{x_i\}_{i=1}^M$, we first map each 3D sample x_i to a latent feature space \mathcal{Z} using a self-supervised point cloud encoder $f_\theta(\cdot)$, such that $z_i = f_\theta(x_i) \in \mathbb{R}^d$. We perform K -means clustering on \mathcal{Z} with $K = 2$ to partition the dataset into two clusters, C_1 and C_2 .

Guided by the Pareto Principle in large-scale datasets, we hypothesize that high-quality samples constitute the statistical majority, whereas noisy or degenerate samples reside in a sparse minority cluster. We select the purified candidate set $\mathcal{D}_{\text{pure}}$ based on a majority-voting mechanism:

$$\mathcal{D}_{\text{pure}} = \arg \max_{C \in \{C_1, C_2\}} |C|, \quad (4)$$

where $|C|$ denotes the cardinality of the cluster. This procedure effectively suppresses the influence of unstable outliers, providing a robust distribution for subsequent selection.

Stage 2: Fine-grained Geometric Representation. After denoising, we seek to construct a final calibration set $\mathcal{C} (|\mathcal{C}| = N)$ that captures both diverse geometric configurations and local statistical variations. We perform fine-grained clustering on the features of $\mathcal{D}_{\text{pure}}$ with $K = N/2$ clusters, denoted as $\{S_k\}_{k=1}^{N/2}$. For each cluster S_k with centroid μ_k , we select two representative samples closest to the cluster centroid, defined as:

$$z_{k,1} = \arg \min_{z \in S_k} \|z - \mu_k\|_2. \quad (5)$$

$$z_{k,2} = \arg \min_{z \in S_k \setminus \{z_{k,1}\}} \|z - \mu_k\|_2. \quad (6)$$

The final calibration set is defined as $\mathcal{C} = \bigcup_{k=1}^{N/2} \{z_{k,1}, z_{k,2}\}$. This strategy ensures that \mathcal{C} not only spans the broad geometric manifold but also encapsulates local variations, thereby enhancing the stability of the estimated quantization parameters.

3.3. Quantization Interval Optimization via Ternary Search

In conventional PTQ frameworks, interval selection is typically treated as an exhaustive grid search over a discrete candidate set $\mathcal{A} = \{\alpha_i\}_{i=1}^N$. This incurs prohibitive $\mathcal{O}(N)$ computational overhead, as each candidate requires a complete quantized forward pass. For large-scale 3D geometry models, this linear complexity becomes a critical calibration bottleneck, with execution times often exceeding 522.6 GPU-minutes per model. To alleviate this, we propose an accelerated interval optimization strategy based on the *unimodality* of the quantization objective.

Unimodality of the Similarity Landscape. We investigate the behavior of the similarity function $\text{Sim}(\mathbf{y}_{\text{FP}}, \mathbf{y}_\alpha)$ across the candidate space \mathcal{A} . As illustrated in Fig. 3, the similarity score exhibits a consistent *near-unimodal* trend for

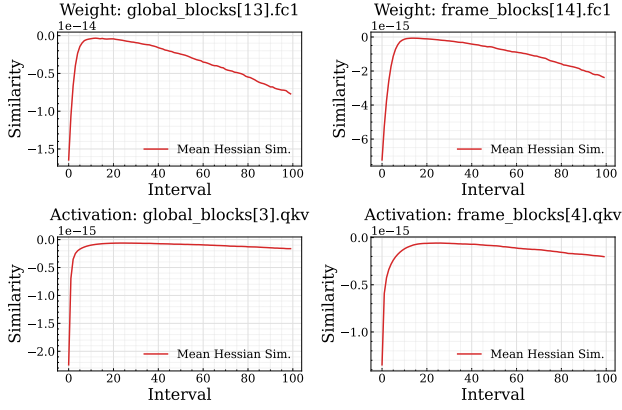


Figure 3. Unimodal behavior of similarity with respect to quantization interval. The similarity between quantized and full-precision outputs is evaluated over a discrete set of interval candidates for both activations and weights. In both cases, the similarity exhibits an approximately unimodal trend, enabling efficient interval search via ternary search.

both weights and activations. This phenomenon is rooted in the fundamental trade-off of quantization: a narrow interval leads to excessive *clipping distortion*, while an overly wide interval increases *rounding noise* by coarsening the quantization step size. The competition between these two error sources naturally induces a unimodal landscape, where a unique global optimum exists.

Ternary Search Solver. Leveraging the unimodal property, we reformulate interval selection as a constrained optimization problem. Instead of a linear scan, we employ a ternary search algorithm to progressively narrow the search boundaries $[L, R]$ within the discrete index range $[1, N]$. At each iteration, we evaluate two interior points m_1 and m_2 :

$$m_1 = L + \frac{R - L}{3}, \quad m_2 = R - \frac{R - L}{3}. \quad (7)$$

By comparing the similarity scores Sim_{m_1} and Sim_{m_2} obtained from the quantized forward passes, the search space is updated as follows:

$$[L, R] \leftarrow \begin{cases} [m_1, R] & \text{if } \text{Sim}_{m_1} < \text{Sim}_{m_2}, \\ [L, m_2] & \text{otherwise.} \end{cases} \quad (8)$$

The search terminates when $R - L \leq \epsilon$, where ϵ is a small convergence threshold (e.g., $\epsilon = 0.0001$). This strategy is applicable to both weight and activation calibration, ensuring broad portability across different layers.

Complexity Analysis. While conventional linear search requires $\mathcal{O}(N)$ evaluations, our ternary search solver reduces the complexity to $\mathcal{O}(\log N)$. In practice, this logarithmic reduction transforms the calibration process from a time-intensive bottleneck into a near-instantaneous operation. Furthermore, our method avoids the sub-optimal local

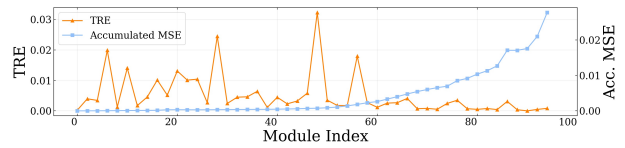


Figure 4. Accumulated MSE and Tail Relative Error across W4A8 quantized Transformer modules. The accumulated MSE is measured at the output of each quantized module along the network depth. Results are reported for a quantized VGGT model with layer-wise calibration applied.

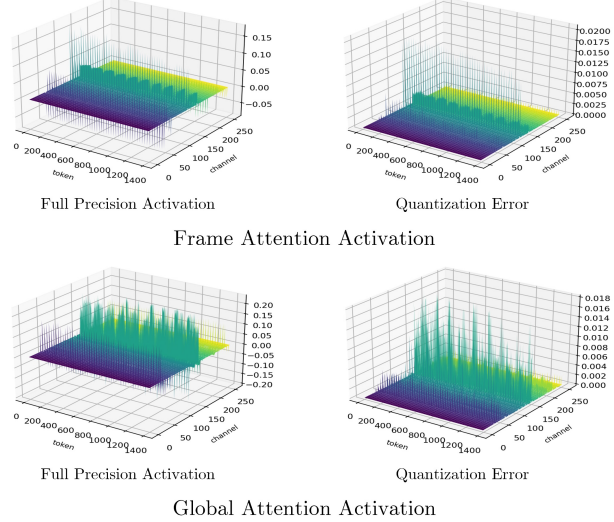


Figure 5. Visualization of activation values and corresponding quantization errors. Each horizontal pair shows the full-precision activations (left) and the corresponding quantization errors (right) for representative attention modules. Both distributions exhibit heavy-tailed characteristics, with large-magnitude activations contributing disproportionately to the observed quantization error.

minima often inherent in coarse grid searches, maintaining high quantization fidelity while significantly accelerating the deployment pipeline.

3.4. TRE-Guided Module-wise Compensation

Despite optimal interval selection, PTQ for deep 3D geometry transformers still suffers from *cascading quantization noise*. Since PTQ follows a sequential calibration paradigm without end-to-end optimization, quantization errors introduced in preceding layers inevitably accumulate and amplify as they propagate through the network hierarchy. As illustrated in Fig. 4, the cumulative error at each transformer block’s output increases monotonically with depth. For dense geometric tasks, these amplified distortions lead to significant structural drift in the inferred 3D space. To mitigate this, we propose **TRE-Guided Module-wise Compensation**, a selective, low-rank correction mechanism.

Low-rank Residual Compensation. We apply compensation to the two core residual submodules in each transformer block: the Attention layer and the MLP layer. To rectify the residual error between the full-precision output \mathbf{y} and its quantized counterpart \mathbf{y}_Δ , we introduce a parallel lightweight branch that is inspired by QwT (Fu et al., 2025). Furthermore, inspired by the observation that quantization error often exhibits low-rank characteristics (Li et al., 2023b), we formulate the compensated output $\hat{\mathbf{y}}_q$ as:

$$\hat{\mathbf{y}}_q = \mathbf{y}_q + \mathbf{U}\mathbf{V}\mathbf{x} + b, \quad (9)$$

where \mathbf{x} is the submodule input, and $\mathbf{U} \in \mathbb{R}^{d \times r}$, $\mathbf{V} \in \mathbb{R}^{r \times d}$ constitute a low-rank adapter with rank $r \ll d$. The optimal compensation matrix $\mathbf{W}_{comp} \approx \mathbf{U}\mathbf{V}$ and bias b is estimated via closed-form linear regression on the calibration set:

$$(\mathbf{W}_{comp}, b) = \arg \min_{\mathbf{W}, b} \|\mathbf{y} - (\mathbf{y}_q + \mathbf{W}\mathbf{x} + b)\|_2^2. \quad (10)$$

To minimize deployment overhead, we apply truncated Singular Value Decomposition (SVD) to \mathbf{W}_{comp} and retain only the r dominant singular components to construct \mathbf{U} and \mathbf{V} . This sequential estimation ensures that each module’s compensation accounts for errors propagated from all preceding layers.

Tail Relative Error (TRE) Gating. While module-wise compensation rectifies local bias, indiscriminate application to all layers incurs unnecessary parameter overhead and risks over-correction. Crucially, as shown in Fig. 5, quantization distortions are not uniformly distributed but are often dominated by high-magnitude activation outliers. Conventional global metrics like MSE fail to capture this sensitivity as they dilute the impact of outliers across the entire feature dimension.

We therefore introduce **Tail Relative Error (TRE)** to identify modules where high-magnitude distortions significantly compromise geometric fidelity. For a module output $\mathbf{y} \in \mathbb{R}^n$, we define the tail index set \mathcal{S} containing the indices of the top- k elements with the largest absolute magnitudes, where $k = \lfloor \rho n \rfloor$ (typically $\rho = 0.01$). The TRE is defined as:

$$TRE(\mathbf{y}, \mathbf{y}_q) = \frac{\sum_{i \in \mathcal{S}} (y_i - y_{q,i})^2}{\sum_{i \in \mathcal{S}} y_i^2 + \epsilon}, \quad (11)$$

where ϵ is a small constant for numerical stability. TRE explicitly quantifies the relative energy distortion concentrated in the long-tailed regions of the activation distribution. We employ TRE as an adaptive gating mechanism: the compensation branch (\mathbf{U}, \mathbf{V}) is activated only if $TRE > \tau$, where τ is a predefined threshold. This selective activation ensures that hardware resources are prioritized for the most error-sensitive modules, preserving geometric consistency with minimal computational footprint.

Table 1. Quantization results on the ETH3D dataset. Best results in each column are highlighted in **bold**. Our method is highlighted in light yellow.

Model	Bit-Width	Method	Acc. \downarrow		Comp. \downarrow		N.C. \uparrow	
			Mean	Med.	Mean	Med.	Mean	Med.
VGGT	W4A8	RTN	0.879	0.868	3.504	2.827	0.543	0.568
		PTQ4ViT	0.669	0.559	1.107	0.770	0.684	0.765
		ERQ	1.010	0.954	2.368	1.978	0.547	0.582
		RepQ	1.144	1.112	2.895	2.311	0.535	0.548
		GPTQ	0.872	0.834	2.686	2.046	0.539	0.563
		Ours	0.492	0.367	0.677	0.446	0.761	0.876
VGGT	W6A6	RTN	0.900	0.804	1.965	1.350	0.572	0.611
		PTQ4ViT	0.389	0.254	0.440	0.276	0.806	0.914
		ERQ	0.598	0.455	0.679	0.358	0.737	0.839
		RepQ	0.946	0.855	2.222	1.547	0.577	0.612
		GPTQ	0.407	0.290	0.549	0.345	0.783	0.889
		Ours	0.334	0.216	0.406	0.226	0.813	0.925
Pi3	W4A8	RTN	1.181	1.178	2.281	1.669	0.522	0.534
		PTQ4ViT	0.413	0.289	0.480	0.307	0.780	0.898
		RepQ	0.976	0.940	3.062	2.514	0.513	0.514
		ERQ	0.869	0.833	2.802	2.173	0.559	0.585
		GPTQ	0.872	0.834	2.686	2.046	0.539	0.563
		Ours	0.392	0.271	0.478	0.308	0.781	0.907
Pi3	W6A6	RTN	1.134	1.135	2.829	2.095	0.525	0.534
		PTQ4ViT	0.221	0.140	0.237	0.136	0.845	0.955
		RepQ	0.888	0.844	2.398	1.853	0.532	0.548
		ERQ	0.293	0.202	0.270	0.141	0.743	0.858
		GPTQ	0.407	0.290	0.549	0.345	0.783	0.889
		Ours	0.209	0.130	0.228	0.131	0.856	0.960

4. Experiments

4.1. Experiment and Evaluation Settings

Base Model. We evaluate VGGT-1B (Wang et al., 2025b) and Pi3 (Wang et al., 2025c), and quantize each model directly from its pre-trained full-precision checkpoint without retraining.

Tasks and Datasets. We mainly evaluate point cloud reconstruction. For calibration, we randomly sample 20 instances from the DTU training split and construct an 8-sample calibration set using our Progressive Calibration Set Construction; this set is used for all experiments. For evaluation, we report reconstruction results on 7Scenes and ETH3D. We also evaluate the prediction of camera parameters on Co3Dv2 to test cross-task robustness.

Quantization Settings. We consider three common low-bit configurations: W4A8, W6A6, and W8A8.

Baseline Methods. We compare with representative PTQ baselines, including Round-to-nearest (RTN), PTQ4ViT (Yuan et al., 2022), RepQ-ViT (Li et al., 2023c), ERQ, and GPTQ (Frantar et al., 2022). For GPTQ, whose original implementation quantizes weights only, we adopt PT4ViT activation quantizer.

For a fair and controlled comparison, we evaluate all meth-

Table 2. Quantization results on the 7Scenes dataset. Best results in each column are highlighted in **bold**. Our method is highlighted in light yellow .

Model	Bit-Width	Method	Acc. \downarrow		Comp. \downarrow		N.C. \uparrow	
			Mean	Med.	Mean	Med.	Mean	Med.
VGGT	W4A8	RTN	0.059	0.038	0.657	0.575	0.586	0.631
		PTQ4ViT	0.046	0.022	0.056	0.022	0.680	0.776
		ERQ	0.077	0.044	0.371	0.273	0.610	0.664
		RepQ	0.078	0.051	0.425	0.334	0.611	0.666
		GPTQ	0.086	0.057	0.422	0.306	0.594	0.646
		Ours	0.028	0.011	0.044	0.015	0.687	0.788
		RTN	0.093	0.055	0.165	0.070	0.637	0.708
Pi3	W6A6	PTQ4ViT	0.023	0.009	0.039	0.015	0.690	0.792
		ERQ	0.048	0.024	0.067	0.029	0.671	0.764
		RepQ	0.127	0.082	0.180	0.075	0.594	0.645
		GPTQ	0.022	0.009	0.038	0.014	0.689	0.792
		Ours	0.021	0.009	0.037	0.014	0.690	0.793
		RTN	0.043	0.033	0.712	0.643	0.497	0.496
		PTQ4ViT	0.027	0.013	0.044	0.014	0.674	0.771
Pi3	W4A8	RepQ	0.069	0.047	0.451	0.344	0.493	0.490
		ERQ	0.068	0.045	0.426	0.326	0.536	0.554
		GPTQ	0.086	0.057	0.422	0.306	0.594	0.646
		Ours	0.026	0.013	0.046	0.016	0.672	0.768
		RTN	0.057	0.043	0.568	0.481	0.503	0.504
		PTQ4ViT	0.018	0.008	0.022	0.009	0.683	0.785
		RepQ	0.096	0.060	0.213	0.087	0.508	0.511
Pi3	W6A6	ERQ	0.021	0.010	0.017	0.006	0.564	0.598
		GPTQ	0.022	0.009	0.038	0.014	0.689	0.792
		Ours	0.017	0.007	0.022	0.009	0.681	0.782

ods under a unified *per-tensor* weight quantization setting. Our method is inherently agnostic to the choice of quantization granularity and can be applied under both per-tensor and channel-wise settings, whereas several baseline methods are originally formulated with channel-wise weights. Allowing channel-wise quantization for these baselines in the main comparison would introduce an inherent advantage due to the additional per-channel scaling flexibility. We therefore standardize all baselines to the per-tensor setting, ensuring that the comparison primarily reflects differences in calibration and error-mitigation strategies rather than quantizer granularity. For completeness, we additionally compare our method with channel-wise variants of these baselines in Appendix D.1.

Implementation Details. Unless otherwise specified, all methods use the same calibration data and inference settings. Additional implementation details, hyperparameters, and calibration configurations are provided in Appendix B.

Metrics. For point cloud reconstruction, we report Acc. and Comp. (lower is better) and N.C. (higher is better). For camera parameter prediction on Co3Dv2, we report AUC at multiple thresholds (A@30/A@15/A@5/A@3; higher is better).

Table 3. Camera parameter prediction results. Best results in each column are highlighted in **bold**. Our method is highlighted in light yellow .

Bit-Width	Method	A@30 \uparrow	A@15 \uparrow	A@5 \uparrow	A@3 \uparrow
W4A8	RTN	0.0041	0.0007	0.0000	0.0000
	PTQ4ViT	0.7622	0.6151	0.2753	0.1363
	GPTQ	0.0334	0.0137	0.0010	0.0005
	ERQ	0.0202	0.0043	0.0006	0.0002
	REPQ	0.0063	0.0006	0.0000	0.0000
	Ours	0.8099	0.6848	0.3975	0.2484
W8A8	RTN	0.8998	0.8190	0.5914	0.4380
	PTQ4ViT	0.9220	0.8592	0.6877	0.5635
	GPTQ	0.9225	0.8608	0.6907	0.5686
	ERQ	0.9014	0.8193	0.5596	0.3906
	REPQ	0.8524	0.7373	0.4379	0.2827
	Ours	0.9252	0.8620	0.6933	0.5723

4.2. Main Results

Quantitative Comparison. We evaluate TAPTQ on point cloud reconstruction across 7Scenes and ETH3D under two quantization settings, W4A8 and W6A6. Results are summarized in Tables 2 and 1, with additional experiments on DTU reported in Appendix D.2. Lower Acc. and Comp. indicate better reconstruction quality, while higher N.C. reflects improved normal consistency.

Overall, TAPTQ consistently improves reconstruction performance across benchmarks and architectures, with larger gains observed under aggressive quantization and on more challenging scenes. On 7Scenes, TAPTQ achieves the best or competitive results on both VGGT and Pi3. Notably, under W4A8, TAPTQ clearly outperforms existing PTQ baselines on VGGT, while under W6A6, where performance becomes saturated, it remains among the top-performing methods without degradation. On ETH3D, TAPTQ delivers more pronounced improvements across both models, highlighting its robustness to complex geometry and severe quantization noise.

Qualitative Comparison. Figure 9 compares the W6A6 reconstruction results produced by PTQ4ViT and TAPTQ on VGGT and Pi3. Under the same quantization setting, TAPTQ better preserves geometric structures and surface continuity. Additional qualitative comparisons are provided in the appendix.

Camera Parameter Prediction. Table 3 reports camera parameter prediction results under W4A8 and W8A8. This task is highly sensitive to quantization. Under W4A8, most baselines collapse, while TAPTQ substantially improves AUC across thresholds. Under W8A8, TAPTQ achieves the best performance.

Table 4. Ablation on calibration set construction. Model: VGGT, dataset: 7Scenes, setting: W4A8. All methods select calibration samples from the same initial pool of 20 DTU training samples. Best results in each column are highlighted in **bold**. Our method is highlighted in light yellow.

Size	Method	Acc. \downarrow		Comp. \downarrow		N.C. \uparrow	
		Mean	Med.	Mean	Med.	Mean	Med.
20	All samples	0.0281	0.0123	0.0452	0.0161	0.6864	0.7873
4	rand (case1)	0.0370	0.0146	0.0580	0.0241	0.6842	0.7835
	rand (case2)	0.0354	0.0158	0.0495	0.0198	0.6864	0.7863
	rand (case3)	0.0310	0.0129	0.0481	0.0163	0.6874	0.7898
	rand (case4)	0.0298	0.0117	0.0456	0.0160	0.6825	0.7823
	rand (case5)	0.0332	0.0134	0.0508	0.0178	0.6851	0.7856
	rand (case6)	0.0307	0.0122	0.0468	0.0165	0.6836	0.7819
8	Stability Score	0.0291	0.0122	0.0470	0.0161	0.6851	0.7852
	Ours	0.0295	0.0121	0.0460	0.0166	0.6868	0.7875
	rand (case1)	0.0300	0.0131	0.0496	0.0177	0.6868	0.7884
16	rand (case2)	0.0342	0.0139	0.0449	0.0158	0.6818	0.7806
	rand (case3)	0.0318	0.0134	0.0478	0.0169	0.6842	0.7841
32	Stability Score	0.0330	0.0137	0.0436	0.0164	0.6811	0.7805
	Ours	0.0264	0.0105	0.0444	0.0147	0.6867	0.7884

Table 5. Ablation on compensation threshold τ under W4A8. Results on 7Scenes.

Strategy	Acc. \downarrow		Comp. \downarrow		N.C. \uparrow		Param. (MB)
	Mean	Med.	Mean	Med.	Mean	Med.	
No comp	0.0457	0.0218	0.0562	0.0222	0.6795	0.7757	608.0799
Full comp	0.0291	0.0117	0.0377	0.0147	0.6863	0.7876	616.9549
$\tau=0.005$	0.0271	0.0110	0.0392	0.0146	0.6835	0.7842	612.2049
$\tau=0.01$	0.0279	0.0110	0.0436	0.0153	0.6868	0.7883	610.3299
$\tau=0.02$	0.0306	0.0125	0.0489	0.0157	0.6872	0.7883	609.3924
$\tau=0.007$	0.0251	0.0102	0.0401	0.0146	0.6878	0.7903	611.3299

4.3. Ablation Study

Effect of Calibration Set Construction. Table 4 compares calibration set construction strategies on 7Scenes under W4A8, using the same initial pool of 20 DTU training samples. *All samples* uses all 20 samples as a high-cost reference; *rand* reports multiple random draws to show variance; *Stability score* filters unstable samples using Appendix A.2 and then performs $K=4$ k-means with proportional sampling.

As shown in Table 4, random selection shows large variance under small budgets. With only 8 samples, our method achieves the best overall performance and even surpasses the 20-sample baseline, which highlights the importance of filtering out noisy samples.

Effect of the Compensation Threshold τ . We further investigate the impact of the compensation threshold τ in the proposed TRE-Guided Compensation Module. Table 5 presents the results on 7Scenes under W4A8. As shown in Table 5, quantization without compensation causes

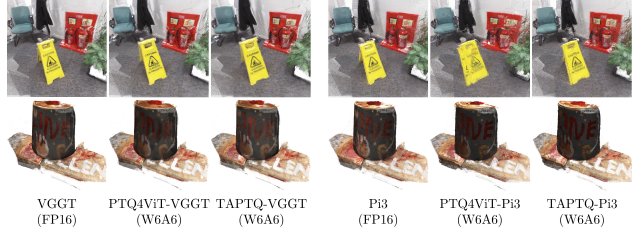


Figure 6. Qualitative Comparison. Visual comparison of W6A6 quantized reconstructions produced by PTQ4ViT and TAPTQ on VGGT and Pi3.

Table 6. Effect of ternary search and module-wise compensation under W6A6. Quantitative results on the 7Scenes dataset that evaluate the reconstruction performance and calibration efficiency. All results report mean values; Time denotes calibration time.

Ternary Search	Error Compens.	Acc. \downarrow	Comp. \downarrow	N.C. \uparrow	Time
✓	✓	0.021	0.035	0.692	168.7 min
✓	✗	0.023	0.040	0.688	161.5 min
✗	✓	0.020	0.036	0.691	529.7 min
✗	✗	0.023	0.039	0.690	522.6 min

a substantial degradation in reconstruction quality. Full compensation recovers performance but may over-correct quantization-insensitive modules. In contrast, TRE-guided compensation provides a better performance by compensating only high-TRE modules. As τ increases from 0.005 to 0.02, the number of compensated modules decreases; $\tau=0.007$ achieves the best overall performance.

Effect of Ternary Search and Compensation. Table 6 evaluates ternary search and module-wise compensation under W6A6. Ternary search replaces exhaustive interval enumeration, substantially reducing calibration time with comparable accuracy. Module-wise compensation further improves reconstruction quality with marginal overhead, indicating that the two components are complementary.

5. Conclusion

We propose **TAPTQ**, a Tail-Aware Post-Training Quantization pipeline tailored for 3D geometry models. TAPTQ combines **Progressive Calibration Set Construction** for stable range estimation under limited calibration budgets, **Quantization Interval Optimization via Ternary Search** to reduce interval calibration cost, and **TRE-Guided Module-wise Compensation** to selectively correct cross-layer error accumulation. Across point cloud reconstruction benchmarks (7Scenes/ETH3D) and camera parameter prediction on Co3Dv2, TAPTQ consistently improves quantized performance under low-bit settings (e.g., W4A8/W6A6/W8A8), with particularly strong gains under aggressive quantization. Ablations further validate the complementarity of ternary

search and TRE-guided compensation, showing improved calibration efficiency and accuracy–consistency trade-offs.

Impact Statement

This paper presents work whose goal is to advance the field of Machine Learning. There are many potential societal consequences of our work, none which we feel must be specifically highlighted here.

References

Banner, R., Nahshan, Y., and Soudry, D. Post training 4-bit quantization of convolutional networks for rapid-deployment. *Advances in neural information processing systems*, 32, 2019.

Barron, J. T., Mildenhall, B., Tancik, M., Hedman, P., Martin-Brualla, R., and Srinivasan, P. P. Mip-nerf: A multiscale representation for anti-aliasing neural radiance fields. In *Proceedings of the IEEE/CVF international conference on computer vision*, pp. 5855–5864, 2021.

Cui, H., Gao, X., Shen, S., and Hu, Z. Hsfn: Hybrid structure-from-motion. In *Proceedings of the IEEE conference on computer vision and pattern recognition*, pp. 1212–1221, 2017.

Feng, W., Qin, H., Wu, M., Yang, C., Li, Y., Li, X., An, Z., Huang, L., Zhang, Y., Magno, M., et al. Quantized visual geometry grounded transformer. *arXiv preprint arXiv:2509.21302*, 2025.

Frantar, E., Ashkboos, S., Hoefer, T., and Alistarh, D. Gptq: Accurate post-training quantization for generative pre-trained transformers. *arXiv preprint arXiv:2210.17323*, 2022.

Fu, M., Yu, H., Shao, J., Zhou, J., Zhu, K., and Wu, J. Quantization without tears. In *Proceedings of the Computer Vision and Pattern Recognition Conference*, pp. 4462–4472, 2025.

Gholami, A., Kim, S., Dong, Z., Yao, Z., Mahoney, M. W., and Keutzer, K. A survey of quantization methods for efficient neural network inference. In *Low-power computer vision*, pp. 291–326. Chapman and Hall/CRC, 2022.

He, B., Yin, L., Zhen, H., Liu, S., Wu, H., Zhang, X., Yuan, M., and Ma, C. Preserving llm capabilities through calibration data curation: From analysis to optimization. *arXiv preprint arXiv:2510.10618*, 2025.

Kerbl, B., Kopanas, G., Leimkühler, T., and Drettakis, G. 3d gaussian splatting for real-time radiance field rendering. *ACM Trans. Graph.*, 42(4):139–1, 2023.

Leroy, V., Cabon, Y., and Revaud, J. Grounding image matching in 3d with mast3r. In *European Conference on Computer Vision*, pp. 71–91. Springer, 2024.

Li, X., Liu, Y., Lian, L., Yang, H., Dong, Z., Kang, D., Zhang, S., and Keutzer, K. Q-diffusion: Quantizing diffusion models. In *Proceedings of the IEEE/CVF International Conference on Computer Vision*, pp. 17535–17545, 2023a.

Li, Y., Gong, R., Tan, X., Yang, Y., Hu, P., Zhang, Q., Yu, F., Wang, W., and Gu, S. Brecq: Pushing the limit of post-training quantization by block reconstruction. *arXiv preprint arXiv:2102.05426*, 2021.

Li, Y., Yu, Y., Liang, C., He, P., Karampatziakis, N., Chen, W., and Zhao, T. Loftq: Lora-fine-tuning-aware quantization for large language models. *arXiv preprint arXiv:2310.08659*, 2023b.

Li, Z., Xiao, J., Yang, L., and Gu, Q. Repq-vit: Scale reparameterization for post-training quantization of vision transformers. In *Proceedings of the IEEE/CVF International Conference on Computer Vision*, pp. 17227–17236, 2023c.

Lin, H., Chen, S., Liew, J., Chen, D. Y., Li, Z., Shi, G., Feng, J., and Kang, B. Depth anything 3: Recovering the visual space from any views. *arXiv preprint arXiv:2511.10647*, 2025.

Lin, J., Tang, J., Tang, H., Yang, S., Chen, W.-M., Wang, W.-C., Xiao, G., Dang, X., Gan, C., and Han, S. Awq: Activation-aware weight quantization for on-device llm compression and acceleration. *Proceedings of machine learning and systems*, 6:87–100, 2024.

Mildenhall, B., Srinivasan, P. P., Tancik, M., Barron, J. T., Ramamoorthi, R., and Ng, R. Nerf: Representing scenes as neural radiance fields for view synthesis. *Communications of the ACM*, 65(1):99–106, 2021.

Nagel, M., Baalen, M. v., Blankevoort, T., and Welling, M. Data-free quantization through weight equalization and bias correction. In *Proceedings of the IEEE/CVF international conference on computer vision*, pp. 1325–1334, 2019.

Nagel, M., Amjad, R. A., Van Baalen, M., Louizos, C., and Blankevoort, T. Up or down? adaptive rounding for post-training quantization. In *International conference on machine learning*, pp. 7197–7206. PMLR, 2020.

Schonberger, J. L. and Frahm, J.-M. Structure-from-motion revisited. In *Proceedings of the IEEE conference on computer vision and pattern recognition*, pp. 4104–4113, 2016.

Shen, Y., Zhang, Z., Qu, Y., Zheng, X., Ji, J., Zhang, S., and Cao, L. Fastvggt: Training-free acceleration of visual geometry transformer. *arXiv preprint arXiv:2509.02560*, 2025.

Tang, C., Ouyang, K., Wang, Z., Zhu, Y., Ji, W., Wang, Y., and Zhu, W. Mixed-precision neural network quantization via learned layer-wise importance. In *European conference on computer vision*, pp. 259–275. Springer, 2022.

Wang, C.-S. B., Schmidt, C., Piekenbrinck, J., and Leibe, B. Faster vggt with block-sparse global attention. *arXiv preprint arXiv:2509.07120*, 2025a.

Wang, J., Chen, M., Karaev, N., Vedaldi, A., Rupprecht, C., and Novotny, D. Vggt: Visual geometry grounded transformer. In *Proceedings of the Computer Vision and Pattern Recognition Conference*, pp. 5294–5306, 2025b.

Wang, S., Leroy, V., Cabon, Y., Chidlovskii, B., and Revaud, J. Dust3r: Geometric 3d vision made easy. In *Proceedings of the IEEE/CVF Conference on Computer Vision and Pattern Recognition*, pp. 20697–20709, 2024.

Wang, Y., Zhou, J., Zhu, H., Chang, W., Zhou, Y., Li, Z., Chen, J., Pang, J., Shen, C., and He, T. π^3 : Permutation-equivariant visual geometry learning. *arXiv preprint arXiv:2507.13347*, 2025c.

Wei, X., Gong, R., Li, Y., Liu, X., and Yu, F. Qdrop: Randomly dropping quantization for extremely low-bit post-training quantization. *arXiv preprint arXiv:2203.05740*, 2022.

Xiao, G., Lin, J., Seznec, M., Wu, H., Demouth, J., and Han, S. Smoothquant: Accurate and efficient post-training quantization for large language models. In *International conference on machine learning*, pp. 38087–38099. PMLR, 2023.

Xie, S., Zhang, W., Tang, C., Bai, Y., Lu, R., Ge, S., and Wang, Z. Mesongs: Post-training compression of 3d gaussians via efficient attribute transformation. In *European Conference on Computer Vision*. Springer, 2024.

Xie, S., Liu, J., Zhang, W., Ge, S., Pan, S., Tang, C., Bai, Y., Zhang, C., Fan, X., and Wang, Z. Sizegs: Size-aware compression of 3d gaussian splatting via mixed integer programming. In *ACM MM*, 2025.

Yao, Y., Luo, Z., Li, S., Fang, T., and Quan, L. Mvsnet: Depth inference for unstructured multi-view stereo. In *Proceedings of the European conference on computer vision (ECCV)*, pp. 767–783, 2018.

Yuan, Z., Xue, C., Chen, Y., Wu, Q., and Sun, G. Ptq4vit: Post-training quantization for vision transformers with twin uniform quantization. In *European conference on computer vision*, pp. 191–207. Springer, 2022.

A. Appendix: Additional Details

A.1. Ternary-Search-Based Quantization Interval Search

Algorithm 1 Ternary-Search-Based Quantization Interval Search

```

Input: raw input  $x_0$ , raw output  $y_0$ , interval candidates  $\{\alpha_i\}_{i=1}^N$ , similarity metric  $\text{Sim}(\cdot)$ , layer function  $\mathcal{F}(\cdot; \alpha)$ , minimum interval  $\epsilon$ 
Output: optimal quantization interval  $\alpha^*$ 
 $L = 1, R = N$ 
repeat
     $m_1 = L + (R - L)/3$ 
     $m_2 = R - (R - L)/3$ 
     $y_{m_1} = \mathcal{F}(x_0; \alpha_{m_1})$ 
     $y_{m_2} = \mathcal{F}(x_0; \alpha_{m_2})$ 
     $S_{m_1} = \text{Sim}(y_0, y_{m_1})$ 
     $S_{m_2} = \text{Sim}(y_0, y_{m_2})$ 
    if  $S_{m_1} < S_{m_2}$  then
         $L = m_1$ 
    else
         $R = m_2$ 
    end if
until  $R - L \leq \epsilon$ 
 $\alpha^* = \alpha_{(L+R)/2}$ 

```

A.2. Stability Score

To quantify the effect of our Stage-1 coarse-grained outlier suppression, we follow the noise-filtering principle of QuantVGTT and compute a stability score that measures the inherent stability of individual samples through feature statistics (used only as an auxiliary diagnostic, not a component of TAPQ). Specifically, for a calibration sample x_i , let $\mathbf{T}_l(x_i) \in \mathbb{R}^{N \times C}$ denote the aggregated token representations at layer l . We first compute the average token-wise feature variance at each layer as

$$v_l(x_i) = \frac{1}{N} \sum_{n=1}^N \text{Var}\left(\mathbf{T}_l^{(n)}(x_i)\right), \quad (12)$$

where $\mathbf{T}_l^{(n)}(x_i) \in \mathbb{R}^C$ denotes the feature vector of the n -th token. The sample-level noise magnitude is then obtained by averaging across layers:

$$\bar{v}(x_i) = \frac{1}{L} \sum_{l=1}^L v_l(x_i), \quad (13)$$

and the stability score is defined as the inverse of the aggregated variance:

$$s_i = \frac{1}{\bar{v}(x_i) + \epsilon}, \quad (14)$$

where L denotes the number of layers considered and ϵ is a small constant for numerical stability. Larger values of s_i correspond to lower feature variance and indicate higher sample stability.

As shown in Fig. 7, when applied to a randomly selected pool of 20 samples, unstable samples are grouped together, indicating that this step effectively filters out noisy data.

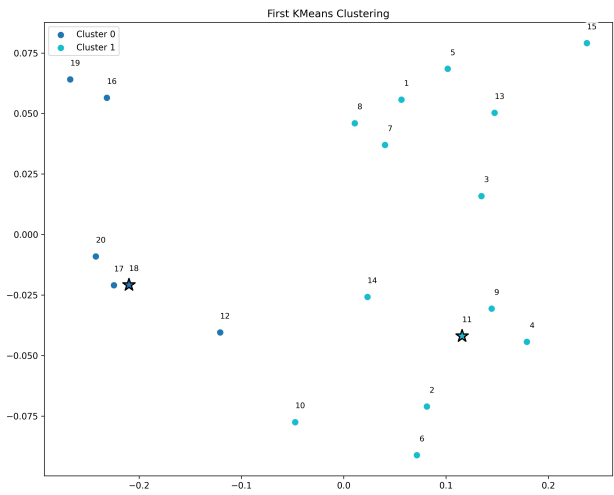


Figure 7. First-stage clustering for noise separation. Each point represents one calibration sample from the initial pool, where the overlaid number indicates its stability score rank (lower rank corresponds to higher stability). A two-cluster K-means is applied to separate unstable samples from relatively stable ones, which are retained for the second-stage clustering.

B. Appendix: Experimental Details

B.1. Calibration Data and Clustering Hyperparameters

Following the main text, we sample 20 instances from the DTU training split as an initial pool, and construct an 8-sample calibration set using **Progressive Calibration Set Construction**. For the clustering procedure, we use $K=2$ in Stage 1 and $K=N/2$ in Stage 2 (where N denotes the target calibration set size).

B.2. TRE-Guided Module-wise Compensation Hyperparameters

We use tail ratio $\rho=0.01$ for **Tail Relative Error (TRE)** and set the compensation threshold to $\tau=0.007$ unless otherwise specified. For the low-rank compensation module, we set the rank to $r=16$.

C. Appendix: Additional Discussion

C.1. Discussion on Calibration Set Selection vs. QuantVGGT

QuantVGGT (Feng et al., 2025) highlights that multi-view calibration in 3D geometry models can be unstable, and proposes model-dependent strategies to filter and sample calibration data. In contrast, our **Progressive Calibration Set Construction** adopts a *model-agnostic* coarse-to-fine clustering strategy in a feature space, balancing outlier suppression and representativeness without relying on any model-specific internal signals; as a result, it is directly applicable across architectures (e.g., VGGT and Pi3). We additionally follow QuantVGGT and report the Stability Score (Appendix A.2) to quantify the effect of Stage-1 coarse-grained outlier suppression; TAPTO itself remains model-independent in the calibration data selection stage.

D. Appendix: More Experiments

D.1. Channel-wise Experiment

Table 7. Channel-wise quantization results. Results on the 7Scenes dataset using the VGGT model. Best results in each column are highlighted in **bold**. Our method is highlighted in light yellow .

Bit-Width	Method	Acc. \downarrow		Comp. \downarrow		N.C. \uparrow	
		Mean	Med.	Mean	Med.	Mean	Med.
W4A8	ERQ (ch-wise)	0.026	0.012	0.043	0.018	0.683	0.783
	RepQ (ch-wise)	0.058	0.027	0.100	0.032	0.661	0.747
	GPTQ (ch-wise)	0.021	0.009	0.033	0.017	0.686	0.788
	Ours	0.028	0.011	0.044	0.015	0.687	0.788
W6A6	ERQ (ch-wise)	0.033	0.014	0.045	0.018	0.675	0.773
	RepQ (ch-wise)	0.037	0.016	0.048	0.019	0.680	0.778
	GPTQ (ch-wise)	0.021	0.009	0.036	0.014	0.691	0.794
	Ours	0.021	0.009	0.037	0.014	0.690	0.793

D.2. Results on DTU

D.3. Qualitative Comparison

Table 8. Quantization results on the DTU dataset. Quantization results on the DTU dataset using the VGGT model. We report mean and median values. Best results in each column (within the same quantization setting) are highlighted in **bold**. Our method is highlighted in light yellow .

Bit-Width	Method	Acc. \downarrow		Comp. \downarrow		N.C. \uparrow	
		Mean	Med.	Mean	Med.	Mean	Med.
W4A8	RTN	8.093	6.168	32.707	20.993	0.586	0.629
	ERQ	7.315	5.296	19.563	8.523	0.634	0.697
	RepQ	10.011	7.740	20.115	7.943	0.610	0.662
	GPTQ	8.117	5.973	32.042	20.285	0.604	0.651
	Ours	1.147	0.648	2.179	0.990	0.682	0.770
W6A6	RTN	7.879	5.748	11.939	3.806	0.653	0.723
	ERQ	1.229	0.704	2.178	1.144	0.684	0.769
	RepQ	10.395	7.445	19.965	10.676	0.605	0.654
	GPTQ	1.204	0.679	2.000	0.935	0.679	0.767
	Ours	1.190	0.671	1.818	0.908	0.678	0.765
W8A8	RTN	1.216	0.729	2.174	1.192	0.687	0.772
	PTQ4ViT	1.136	0.665	2.043	1.135	0.691	0.776
	ERQ	1.196	0.715	2.189	1.256	0.693	0.778
	GPTQ	1.166	0.686	2.081	1.182	0.692	0.777
	Ours	1.153	0.673	2.025	1.135	0.692	0.776

Table 9. Quantization results on the DTU dataset. Quantization results on the DTU dataset using the Pi3 model. We report mean and median values. Best results in each column (within the same quantization setting) are highlighted in **bold**. Our method is highlighted in light yellow .

Bit-Width	Method	Acc. \downarrow		Comp. \downarrow		N.C. \uparrow	
		Mean	Med.	Mean	Med.	Mean	Med.
W4A8	RTN	10.099	7.670	17.295	4.441	0.496	0.494
	PTQ4ViT	2.259	1.301	2.346	0.740	0.682	0.768
	RepQ	8.769	6.654	15.075	2.680	0.501	0.501
	ERQ	8.437	6.272	18.061	5.838	0.532	0.550
	GPTQ	8.117	5.973	32.042	20.285	0.604	0.651
W6A6	Ours	1.759	0.960	2.239	0.663	0.677	0.754
	RTN	10.785	8.225	18.575	5.908	0.498	0.497
	PTQ4ViT	2.557	1.496	2.174	0.769	0.681	0.767
	RepQ	8.327	6.037	14.617	3.167	0.517	0.526
	ERQ	1.710	0.900	1.623	0.566	0.540	0.561
W8A8	GPTQ	1.204	0.679	2.000	0.935	0.679	0.767
	Ours	1.576	0.845	1.999	0.632	0.669	0.754
	RTN	1.721	0.933	2.255	0.667	0.676	0.763
	PTQ4ViT	1.177	0.648	1.767	0.596	0.670	0.756
	RepQ	1.958	1.099	1.870	0.618	0.597	0.649
	ERQ	1.254	0.676	1.538	0.556	0.617	0.679
	GPTQ	1.166	0.686	2.081	1.182	0.692	0.777
	Ours	1.154	0.637	1.753	0.605	0.669	0.755

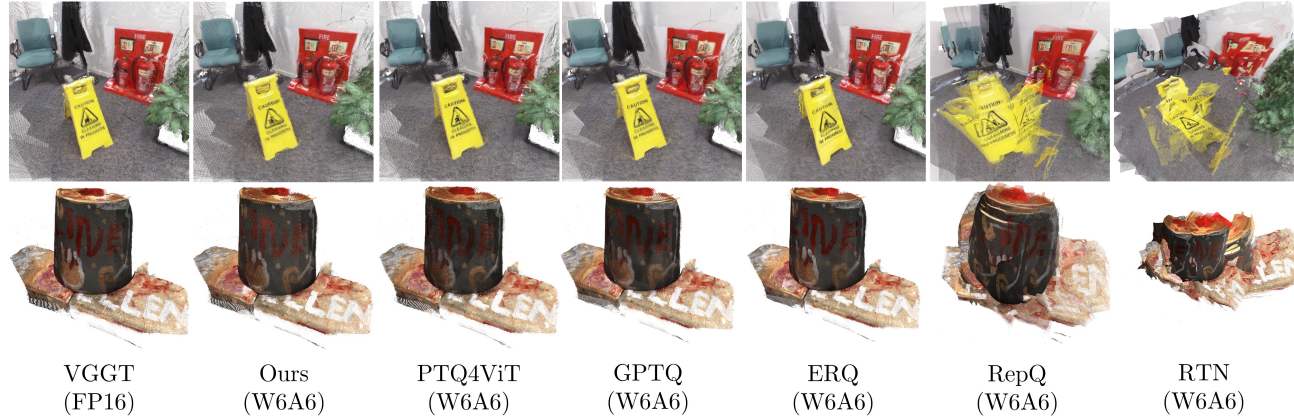


Figure 8. Qualitative Comparison on VGGT.

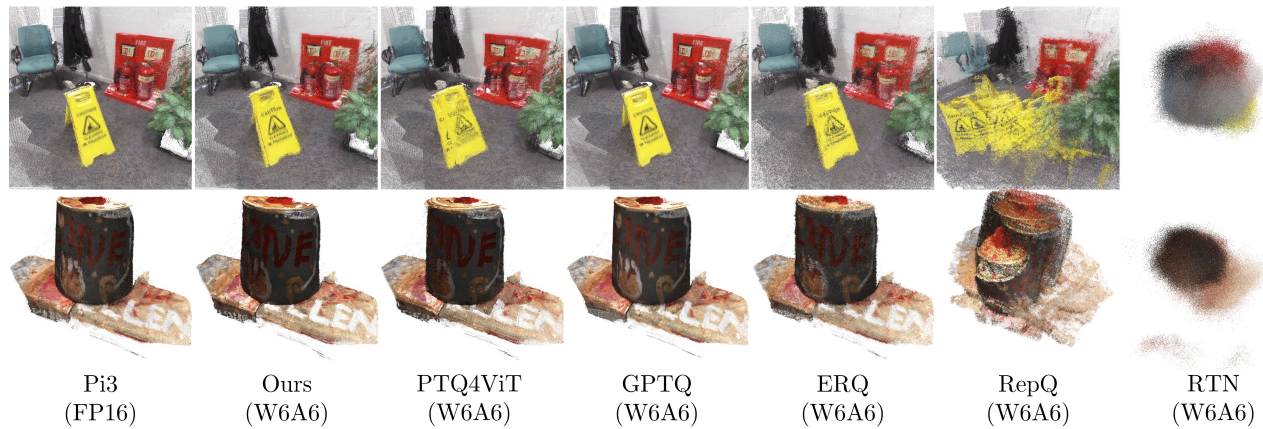


Figure 9. Qualitative Comparison on Pi3.